SCIENCE CHINA
Earth Sciences

•RESEARCH PAPER•

February 2020 Vol.63 No.2: 257–266
https://doi.org/10.1007/s11430-018-9362-6

APOD mission status and preliminary results

Geshi TANG[1,2*], Xie LI[2], Jianfeng CAO[2], Shushi LIU[2], Guangming CHEN[2], Haijun MAN[2], Xiaomin ZHANG[3], Sihan SHI[3], Ji SUN[3], Yongping LI[4] & Andres CALABIA[1]

[1] *Nanjing University of Information Science & Technology (NUIST), Nanjing 210044, China;*
[2] *Aerospace Flight Dynamics Laboratory (AFDL), Beijing Aerospace Control Center (BACC), Beijing 100094, China;*
[3] *China Spacesat Co. Ltd., Beijing 100094, China;*
[4] *National Space Science Center (NSSC), Chinese Academy of Sciences, Beijing 100190, China*

Received November 18, 2018; revised April 17, 2019; accepted April 23, 2019; published online June 3, 2019

Abstract On September 20th, 2015, twenty satellites were successfully deployed into a near-polar circular orbit at 520 km altitude by the Chinese CZ-6 test rocket, which was launched from the TaiYuan Satellite Launch Center. Among these satellites, a set of 4 CubeSats conform the atmospheric density detection and precise orbit determination (APOD) mission, which is projected for atmospheric density estimation from *in-situ* detection and precise orbit products. The APOD satellites are manufactured by China Spacesat Co. Ltd. and the payload instruments include an atmospheric density detector (ADD), a dual-frequency dual-mode global navigation satellite system (GNSS) receiver (GPS and Beidou), a satellite laser ranging (SLR) reflector, and an S/X-band very long baseline interferometry (VLBI) beacon. In this paper, we compare the GNSS precise orbit products with co-located SLR observations, and the 3D orbit accuracy shows better than 10 cm RMS. These results reveal the great potential of the onboard micro-electro-mechanical system (MEMS) GNSS receiver. After calibrating ADD density estimates with precise orbit products, the accuracy of our density products can reach about 10% with respect to the background density. Density estimates from APOD are of a great importance for scientific studies on upper atmosphere variations and useful for model data assimilation.

Keywords Atmospheric density, Low Earth orbit (LEO), Precise orbit determination (POD)

Citation: Tang G, Li X, Cao J, Liu S, Chen G, Man H, Zhang X, Shi S, Sun J, Li Y, Calabia A. 2020. APOD mission status and preliminary results. Science China Earth Sciences, 63: 257–266, https://doi.org/10.1007/s11430-018-9362-6

1. Introduction

Precise orbit determination (POD) and orbit prediction of Low Earth Orbit (LEO) objects, including active satellites and debris, are very important for collision avoidance, orbit maneuvers, and rendezvous and docking in space. However, these applications are still under technical development for accurate and reliable use, and it presents a great challenge for spacecraft operators. Main key reason is the limited capability for atmospheric density modeling at LEO (e.g. Storz et al., 2005; Bowman et al., 2008; Xu et al., 2011; Chen et al., 2014), which results in miss-modeled aerodynamic drag perturbations in LEO POD.

At LEO, atmospheric density variations are mainly driven by the rapid heating changes from the variable solar ultraviolet irradiance, joule heating from electric currents and precipitation of energetic particles in Earth's magnetosphere under different solar wind and interplanetary magnetic field (IMF) conditions, and variations derived from waves originated in the lower atmosphere, which propagate upward (Emmert, 2015). These complex phenomena and the mechanism of atmospheric density variations have been a subject of recent international interest (e.g., Qian and Solomon, 2012).

* Corresponding author (email: tanggeshi@nuist.edu.cn)

During last decades, several empirical and physical models have been developed to describe the complex variability and coupled processes in the upper atmosphere. Unfortunately, due to limited observables and difficulties for modeling, the standard deviation of the most representative models such as NRLMSISE-00, MSISE-90, and Jacchia-70 provide estimates at a relative accuracy of 23% to 42% (with respect to the background density) at the altitude range of 400–800 km (Picone et al., 2002), and the last update of the Jacchia series, Jacchia-Bowman 2008 (JB2008), which includes new solar indices, a new semiannual variation fitting, and a new geomagnetic index, can provide standard deviations of approximately 9–10% at 400 km (Bowman et al., 2008). More recently, the DTM-2013 model has shown to be more accurate than the JB2008 at all altitudes (Bruinsma, 2015). However, model improvements are still necessary, in particular below 300 km and above about 800 km, for which the complete density database is very sparse. Improving the current accuracy of the models is a very challenging task and requires high-quality observations (direct or indirect) with sufficient spatial and temporal resolutions and coverage.

Many techniques have been developed since 1960s to measure thermosphere density, including orbit-derived density, accelerometer-derived density, neutral mass spectrometers, pressure gauge, and ultraviolet remote sensing, among others (Emmert, 2015). Of particular interest, the CHAMP, GRACE and GOCE missions (e.g., Calabia and Jin, 2016; Bruinsma et al., 2014; Doornbos et al., 2010; Sutton et al., 2005) have generated unprecedented volume of high-quality estimates of thermospheric neutral mass density, and have made a great contribution for progresses in upper atmosphere research and modeling. However, a more extensive spatiotemporal coverage is needed to reach the required accuracy of models for practical applications (e.g., POD, re-entry calculations). This is due to the highly complexity and variability of the upper atmosphere estate under solar activity conditions.

Unfortunately, the very expensive schemes for sensing thermospheric neutral mass density through ordinary satellites limit the availability and spatiotemporal coverage of observables. However, the rapid development of micro-electro-mechanical systems and micro- and nano- satellite technologies, such as CubeSat, which includes a miniaturized atmosphere detection payload and a MEMS GNSS receiver, has offered a great new opportunity to detect atmospheric density in a more extensive spatiotemporal coverage, and with a relatively very low cost. The atmospheric density detection and precise orbit determination (APOD) CubeSat project was proposed in 2015 to investigate atmospheric neutral density by technology of *in-situ* miniaturized onboard instrumentation atmospheric density detecter (ADD) and POD-based density derived from MEMES GNSS receiver. In the APOD project, since the ADD *in-situ* detected density and the POD-derived density are completely independent methods, the calibration of instruments and validation of observables can provide a reliable representation of the real upper atmosphere state.

2. Satellites and payload overview

In the APOD mission, there are a nano-satellite (APOD-A) and three pico-satellites (APOD-B/C/D). The four satellites fly in a near-polar circular orbit with an inclination of about 97°. The satellites were launched to an initial orbit of 520 km altitude. After two weeks, the APOD-A descended to an altitude of 470 km. The lifetimes of these four CubeSats were set for 12 month, but depending on space weather conditions the orbit lifetime can be extended up to 3–5 years. At present, the average altitude of satellite orbit is about 450 km, and all kinds of payloads (except dual-frequency GNSS receiver) are running normally. Routine data collection is being carried out and atmospheric density measurement data have been accumulated for more than two and a half years.

In order to obtain atmospheric density by *in-situ* detectors and POD, the payloads include a dual-frequency GNSS receiver, an ADD, a SLR reflector, and two VLBI beacons (Figure 1). The overview of the APOD mission and the carrying payloads are listed in Table 1. Since APOD-B/C/D

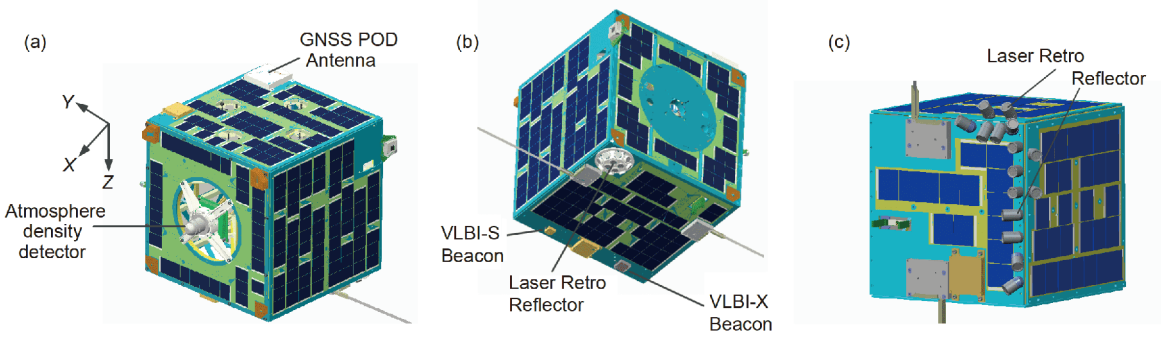

Figure 1 Physical layout of the APOD satellites with the location of scientific instruments. (a) Front side view of APOD-A with location of instruments; (b) bottom side view of APOD-A with location of instruments; (c) bottom side view of APOD-B/C/D with location of Laser Retro-Reflector instruments.

Table 1 The parameters of APOD

			APOD-A	APOD-B/C/D
Satellite system	Physical parameters	Mass	25.88 kg	9.6 kg
		Dimension (body-fixed coordinates) (mm)	391×398×398	263×246×246
		Area to mass ratio (m^2 kg^{-1})	0.00612	0.00630
	Electrical power	Power consumption (W)	19	11
		Payload power (W)	5	3
	AOCS	Stabilized mode	Three-axis attitude stabilized, earth pointing; Spin stabilized if necessary	
		Attitude measuring	Sun sensor, magnetometers and gyroscope	
		Attitude control	Magne-torquers and momentum wheels	
		Attitude determination accuracy (°)	1	
		Pointing accuracy (°)	3	5
		Attitude stability (° s^{-1})	1	
	Data storage	RAM for GNSS (MB)	60	
		RAM for atmosphere density (MB)	3	–
	RF communication	Uplink	S-band, data rate is 2000 bit/s UHF-band, date rate is 1200 bit/s	
		Downlink	S-band, data rate is 16384 bit/s VHF-band, data rate is 19200 bit/s	
Orbit	Mission orbit	Semi-major axis (km)	470	530
		Inclination (°)	97.49	
		Local time of descend node	6:300	6:10
		Expected lifetime (year)	≥1	
Payload system	GNSS receiver	Mode	GPS/BDS	
		GPS Frequency (MHz)	L1:1575.42, L2:1227.60	
		BDS Frequency (MHz)	B1:1561.098, B3:1250.618	
		Sampling rate (s)	8	
	VLBI beacon	S-Band Frequency (MHz)	2262.01–2267.15	–
		X-Band Frequency (MHz)	8424.02–8431.66	–
	Atmosphere density detector	Pressure Range (Pa)	1.0^{-7}–1.0^{-2}	
		Temperature Range (°C)	−20–60	–
		Pressure resolution (Pa)	1×10^{-7}	–
		Sampling rate (science data/instrument status)	1/8 per second	–
		Mass	700 g	
		Power	1 W	
	Laser retro reflector	Type	Pyramid	Mounted on bottom surface dispersedly (See Figure 2)
		Number of cube corner prisms	9	11
		Free aperture of the front face (mm)	100±0.2	10±0.2

are too small to carry an ADD, this paper only covers the results from APOD-A.

The ADD was designed by the National Space Science Center (NSSC) of China. Basically, it is a space-borne sensor which performs *in-situ* temperature and pressure measurements. The ADD is composed by 4 subsystems: a Bayard-Alpert gauge, a thermometer sensor, a spherical gold-plated stainless steel antechamber with a knife-edged orifice inlet, and the electronics unit. Besides the electronics unit, the former subsystems are covered by the steel antechamber (Qin et al., 1990). The ADD is mounted on the front-side of the satellite, in along (+X) direction (Figure 1), the earth-pointing 3-axis stabilization guarantees that aperture can always be oriented to the incoming atmospheric flow.

Main technical specifications of ADD are listed in Table 1. According to ADD's measuring range, pressure and temperature estates and derived density estimates only can be detected from 550 to 120 km.

Since the deployment of APOD in 2015/09/20 until now, the ADD has been working well but the GNSS receivers had performance issues after 2 months of continuous measurements. Though, the GNSS-POD experiment only can be performed during these two months data, and additional orbit products are employed for long-term density calibration, such as Two Line Element (TLE) products (Picone et al., 2005). TLE products used to derive TLE-based density estimates can be accessed from the North American Aerospace Defense Command (NORAD) available at https://www.celestrak.com/NORAD/elements/.

3. Methodology of *in-situ* density observations

3.1 Basic principle of *in-situ* density measurements

The principle of the ADD is depicted in Figure 2. When the gas to be measured enters the chamber through the inlet, a volume of charged particles will be firstly captured by the accommodation panel, and the neutral components will strike the chamber walls and accommodate to temperature of the chamber walls. Hence, the temperature of the gas in the chamber can be measured by thermometer sensor. At the same time, gas molecules will be partially ionized by a stream of electrons emitted from a hot filament, and the resulting ions will be collected by an electrode. In this scheme, the pressure is proportional to the ratio of collected ion current times the ionizing electron current, which is described as

$$P = K\frac{I_e}{I_i}, \tag{1}$$

where I_e is the emission of electron current, I_i is the ions' current, P is the pressure of the gas, and K is the calibration coefficient provided by a ground-based pressure calibration, procedure which needs to be performed before mission launch. A biased grid electrode is also utilized to accelerate electrons such that it moves back and forth between grids and collect electrons for increase ionization efficiency. The intrinsic linearity of this gauge over many orders of magnitude in pressure makes it well-suited for thermosphere estate sensing (Clemmons et al., 2009).

According to kinetic molecular theory, the molecular thermal motion of the upper atmosphere is governed by Maxwell distribution law of velocity as follows:

$$f(v_x, v_y, v_z) = 4\pi\left(\frac{m}{2\pi kT}\right)^{3/2} \cdot V^2 \cdot \mathrm{e}^{-\frac{m\left(v_x^2+v_y^2+v_z^2\right)}{2kT}}, \tag{2}$$

where k is Boltzmann constant, V is the velocity of gas molecular thermal motion, m is the average molecular weight, and T the temperature of the gas. Then, the number density of gas N, flowing on the unit area per unit time, can be obtained by integrating eq. (2). Under the assumption that the number of gas molecules flowing out of the antechamber of detector is the same with entering gas molecules (Qin et al., 1990),

$$N_{\mathrm{in}} = N_{\mathrm{out}}. \tag{3}$$

Clemmons et al. (2009) deduced the equation of atmosphere number density as follows by virtue of temperature and pressure observations in the detector:

$$N_a = P_g(2k\pi m_1)^{-1/2}\left(\frac{1}{T_g}\right)^{1/2}\frac{1}{v\cos\theta}, \tag{4}$$

where $v\cos\theta$ is the velocity of satellite relative to atmosphere, m_1 is the molecular mass of gas. Eq. (4) indicates that number density of the thermosphere estate can be derived by measuring the wall temperature of the antechamber (T_g) and the pressure in the antechamber (P_g). It also should be noted that the above derivation is only valid under free-molecular flow conditions. Hence, the mass density of atmosphere can be written as:

$$\rho = N_a \times m_2, \tag{5}$$

where m_2 is the averaged molecular mass of the atmosphere. Since the payload does not include spectrometer for gas composition, the averaged molecular mass has to be estimated using an atmospheric model, as for example NRLMSIS00.

3.2 Data processing

Following the theoretical basis presented in previous section, since the ADD measures the voltage which represents the temperature and pressure of the gas in the chamber, a laboratory tests can provide the fitting parameters to obtain actual temperature and pressure estates from observed vol-

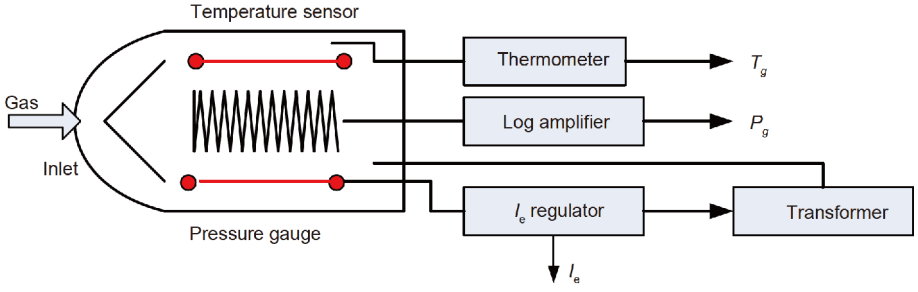

Figure 2 The schematic diagram of working principle for atmospheric density detector.

tage variations. Then, the number density of atmosphere can be calculated using eq. (4). Li et al. (2018) provides the fitting parameters and related uncertainty for temperature and pressure estimation (Figure 4 in Li et al., 2018). As mentioned above, due to the lack of a spectrometer for the measurement of species, we employ the NRLMSIS00 model for the averaged molecular mass, which provides and approximated error of about 15%. Then, in this scheme, the resulting error of ADD density estimates can reach up to 19.08% (Li et al., 2018). The following points provide more details on our data processing scheme:

(1) Temperature and pressure calculation. From original telemetry data, expressed by voltage, the values are transformed to physical quantities in Kelvin and Pascal units using fitting parameters given by Table 2 of Li et al. (2018). The fitting equation, correlation coefficients, and RMS are also listed in the same table. The fitting parameters are obtained by experiments on ground.

(2) Determination of satellite state and attitude. In order to get N_a, the velocity and angle of attack of the satellite must be known in advance. This can be obtained from orbit determination and telemetry parameters. The accuracy of attitude pointing is less than 3°. The effect induced by attitude variations can be neglected.

(3) Calculation of mass density. Thermospheric neutral mass density estimates are obtained following the procedure mentioned above. The averaged molecular mass of the atmosphere at specific altitude is estimated by NRLMSISE00 model as follows:

$$m_2 = \frac{\rho_m}{N_m}, \tag{6}$$

where ρ_m is the mass density calculated by NRLMSIS00 model, and N_m is the overall number density of all 7 species calculated by NRLMSIS00 model.

3.3 Calibration method and results

Drag-derived density estimates from LEO satellites is the most common and direct method to obtain atmospheric estate of the thermosphere. The basic principle of this method is the reduction of the orbital semi-major axis due to atmospheric drag acceleration. Although the perturbing force from the non-spherical gravitational field of Earth is larger than the drag force, it is more accurate and stable than the atmospheric drag. Density retrieval through the reduction of the orbital semi-major axis method is performed from TLE orbital elements (Picone et al., 2005). In addition, Sang et al. (2012) proposed a derivation method from precise orbit, which can provide a retrieval of densities with a high temporal resolution (hourly level). In this manuscript, due to the failure of GNSS receiver on Jan. 2016, and the consequent 2 months of precise orbit data, the long term calibration of ADD is performed from TLE-derived densities. In the following section, GNSS-POD density estimates are plotted with TLE-estimates for comparison.

Density estimates on time t can be derived through the following equations,

$$\rho_o(t_{ik}) = \frac{\frac{2}{3}\mu^{-2/3} n_M(t_{ik})}{n_M^{1/3} B \int_{t_i}^{t_k} F v^3 \mathrm{d}t} \approx \frac{\frac{2}{3}\mu^{-2/3} n_M(t_{ik})}{n_M^{1/3} B \sum_{t_i}^{t_k} F v^3 t}, \tag{7}$$

where μ is the gravitational coefficient, n is the mean motion, t_i and t_k correspond to start and end epochs of TLEs, respectively, v is the velocity of satellite, and F is the wind factor, which is described as

$$F = \frac{|v - v_w|^2}{|v|^2} \hat{e}_{v-v_w} \hat{e}_v, \tag{8}$$

where v_w is the wind velocity calculated by the Horitzontal Wind Model (Hedin et al., 1991), $\hat{e}_{v-v_w}$ is the velocity unit vector of satellite relative to wind velocity.

According to eq. (7), thirteen months of density estimates since December 2015 have been computed and compared with the NRLMSISE00 model. The corresponding ratio of differences is plotted in Figure 8 of Li et al. (2018). Figure 8 of Li et al. (2018) showed an obvious bias during the second half of the year 2015, with generally relative lower values for ADD estimates during periods of low solar flux irradiance. The statistical result showed a standard deviation of about 24.3% for the ratio of differences.

In order to provide a reliable calibration parameters of *in-situ* ADD density estimates, the time-series is compared to TLE-based estimates through a linear function ($y=ax+b$) and a quadratic polynomial ($y=ax^2+bx+c$) by fitting the scattered data. Then, a set of calibration coefficients is provided.

The 2-days average of *in-situ* ADD density estimates from December 2015 to December 2016 are compared to TLE-derived estimates and plotted in Figure 9 in Li et al. (2018). The linear and quadratic polynomial fitting are plotted in the same figure. Correlations statistics and coefficients of the fitting are presented in Table 4 of Li et al. (2018). It can be seen that the correlation statistics reaches the value of 0.943, and with minor differences between the two fitting methods. The final resolution of density products is 1 Hz. From Table 4 and Figure 9 in Li et al. (2018), the standard deviation of calibrated density estimates is about 10^{14} kg m^{-3}, and the absolute density value about 10^{-13} kg m^{-3}, being about an accuracy of 10% with respect to the background density.

4. Preliminary results

4.1 POD and orbit-derived mass density

Since the launch of the APOD mission in 2015, platform and payloads in-orbit commissioning finished, and the APOD is currently in normal operation status. The GNSS-POD products are obtained through GPS L1/L2 carrier phase mea-

surements using the double differencing method. The data rate is about 1/8 Hz with possible losing of carrier phase measurements. POD products are computed using National University of Defense Technology Orbit Determination Toolkit (NUDTTK) software (Gu et al., 2017). The orbit precision is validated by independent measurements of SLR.

The international laser ranging service (ILRS) (Pearlman et al., 2002; Gurtner et al., 2005) provides SLR measurements for the APOD satellites. BACC is responsible for guiding the SLR station with satellite prediction files provided in consolidated prediction format (CPF) to ILRS. More than 4000 normal-point data have been accessed since the first measurement on 2nd, October 2015, by CHAL, SHA2 SLR stations. The six SLR stations that supported APOD mission are shown in Figure 12 in Gu et al. (2017). The SLR measurements are used for an independent validation of GNSS-POD products. The APOD satellites in the ILRS frame are named as PN-1A, -1B, -1C, -1D (in the ILRS SLR mission application support in 2014, the project was not named as APOD yet, so the satellites were named as PN-1A/B/C/D in the request application form). The detailed description of LRR (laser retro reflector) and measurement condition of APOD satellites is described on ILRS website: http://ilrs.gsfc.nasa.gov/missions/satellite_missions/future_missions/pn1a_general.html. ITRF2008 coordinates were used for the SLR stations (Altamimi et al., 2011), the CoM offset of the LRR array was corrected according the parameter described on the ILRS website. The normal point data residuals were larger than 30 cm, and elevation angles less than 15° were removed.

The overlapping employed for validating the GNSS-POD orbit solution of APOD-A comprises 6 h between two consecutive solutions of 30 h. The differences in the overlapping period are employed as an indicator of quality. The averaged 3D RMS of differences reaches 4.59 cm (Figure 14 in Gu et al., 2017) and the average RMS of the SLR residuals for the dual-frequency orbit solutions can be 7.71 cm (Figure 13 in Gu et al., 2017).

In order to provide a long-term calibration of ADD density estimates and circumvent the failure of the GNSS receiver, we derived mass density estimates from the TLE products. In Figure 3, twelve days are plotted to compare density estimates from the 2-month when the GNSS receiver was operative. In this figure, GNSS-POD and TLE derived mass density estimates are plotted together. The results show that GNSS-POD derived mass density estimates have more detail, and the TLE estimates follow an averaged value, which is optimal for ADD calibration.

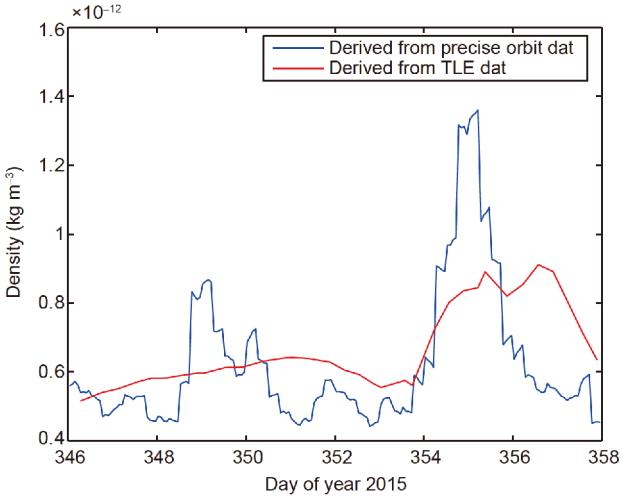

Figure 3 GNSS-POD and TLE derived mass density estimates.

4.2 Comparison between ADD estimates and models

In this section, we compare the TLE-calibrated ADD density estimates with the NRLMSISE-00 and JB2008 models. The results in Li et al. (2018) compare the NRLMSISE-00 density estimates with the daily averaged values of ADD densities using both fitting methods linear and quadratic. The residuals of linear fit have a mean value of -4.10×10^{-14} kg m^{-3} and a standard deviation of 6.58×10^{-14} kg m^{-3}, while the residuals of the quadratic fit provide a mean value of -3.38×10^{-14} kg m^{-3} and a standard deviation of 6.94×10^{-14} kg m^{-3}. Li et al. (2018) also provides the relative errors with respect the background density, which mean values reach 10.1% and 5.2% for the linear and quadratic fitting, respectively, and the relative standard deviation 18.2% and 17.1%, respectively. The results indicate that the quadratic fitting is more convenient for calibration. In addition, their results found an obvious half-year periodic variation of the relative errors and a systematic deviation after 300 days.

In order to isolate possible periodic errors in the empirical density model (which may cause the half-year periodic variation of relative errors), we compare the ADD densities with the JB2008 semi-empirical model. The relative errors with JB2008 are shown in Figure 11 of Li et al. (2018). The mean values show 0.6% and 3.9%, and the standard deviation 14.9% and 16.9%, respectively for the linear and the quadratic fit. In this case, the linear fit shows better results than the quadric fit. Since the JB2008 empirical model updated a half-year periodic variation (Bowman et al., 2008), there is no obvious periodic variations at this frequency. Note also that the absence of the systematic bias shown in Figure 10 in Li et al. (2018). Therefore, the results show that TLE-calibrated ADD density estimates confirm the improvement of JB2008 in representing the half-year periodic variation.

4.3 Demonstration of neutral density variation using APOD data in the Polar Region

During geomagnetic storms, solar energy input primarily

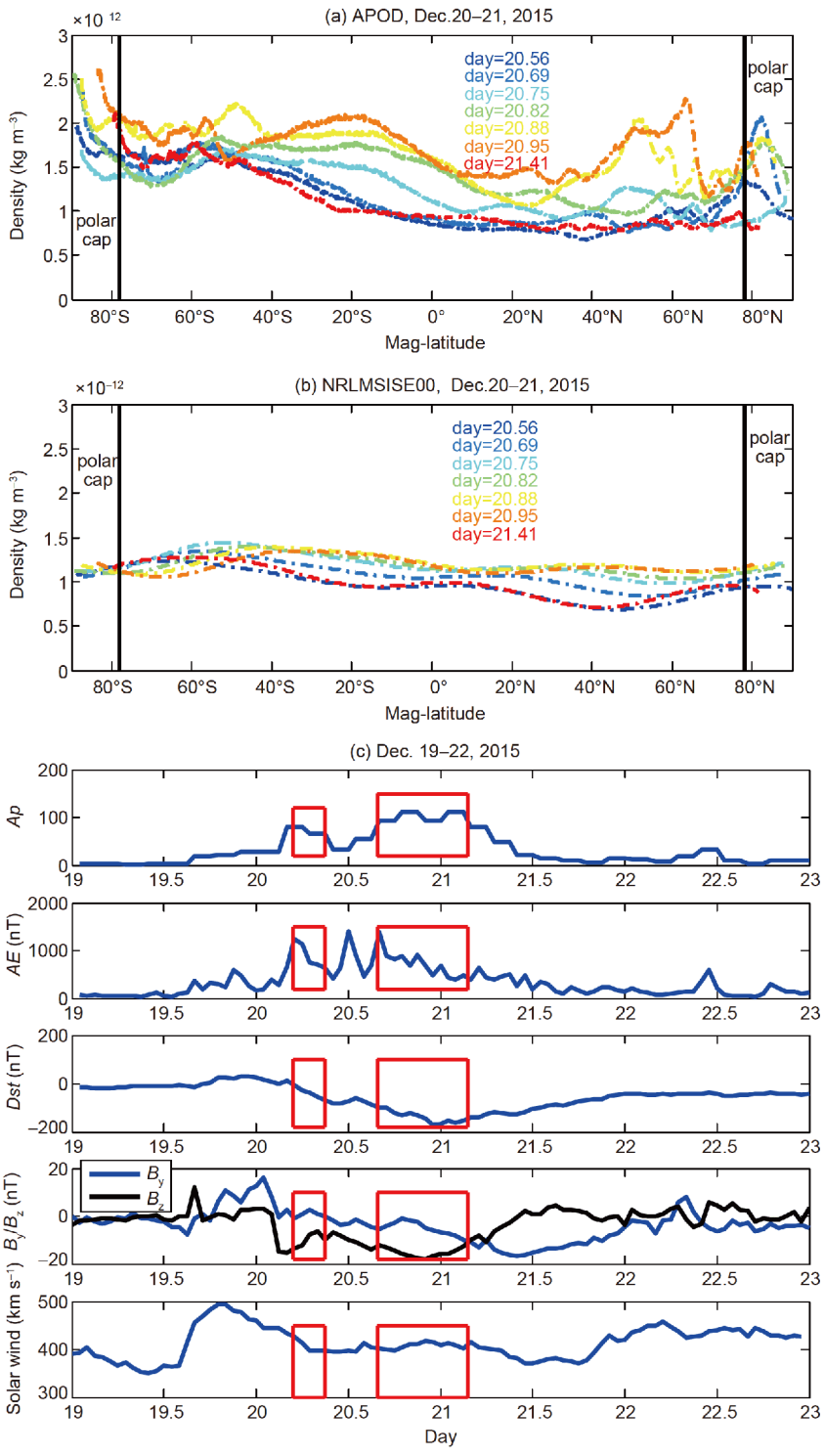

Figure 4 (a) Density variation observed by APOD in several orbits on December 20–21, 2015, (b) density at the same times and locations as (a), calculated by the NRL-MSISE00 model, (c) the geomagnetic and space weather indexes during the geomagnetic storm of December, 2015.

deposited in the aurora area acts in the form of Joule heating and energetic particles precipitation, causing thermosphere density enhancement and subsequently transfer to lower latitudes (Sutton et al., 2005). During last decades, high-latitude neutral-density variations during geomagnetic storms have been explored in gran extent using accelerometer-based estimates from, e.g., CHAMP and GRACE (Calabia and Jin, 2017; Bruinsma et al., 2004; Liu and Lühr, 2005). Such effects on thermosphere dynamics produce drag-perturbations on LEO satellites (Willis et al., 2005). The scientific community has revealed the important effects of thermosphere density variations during geomagnetic storms on LEO sa-

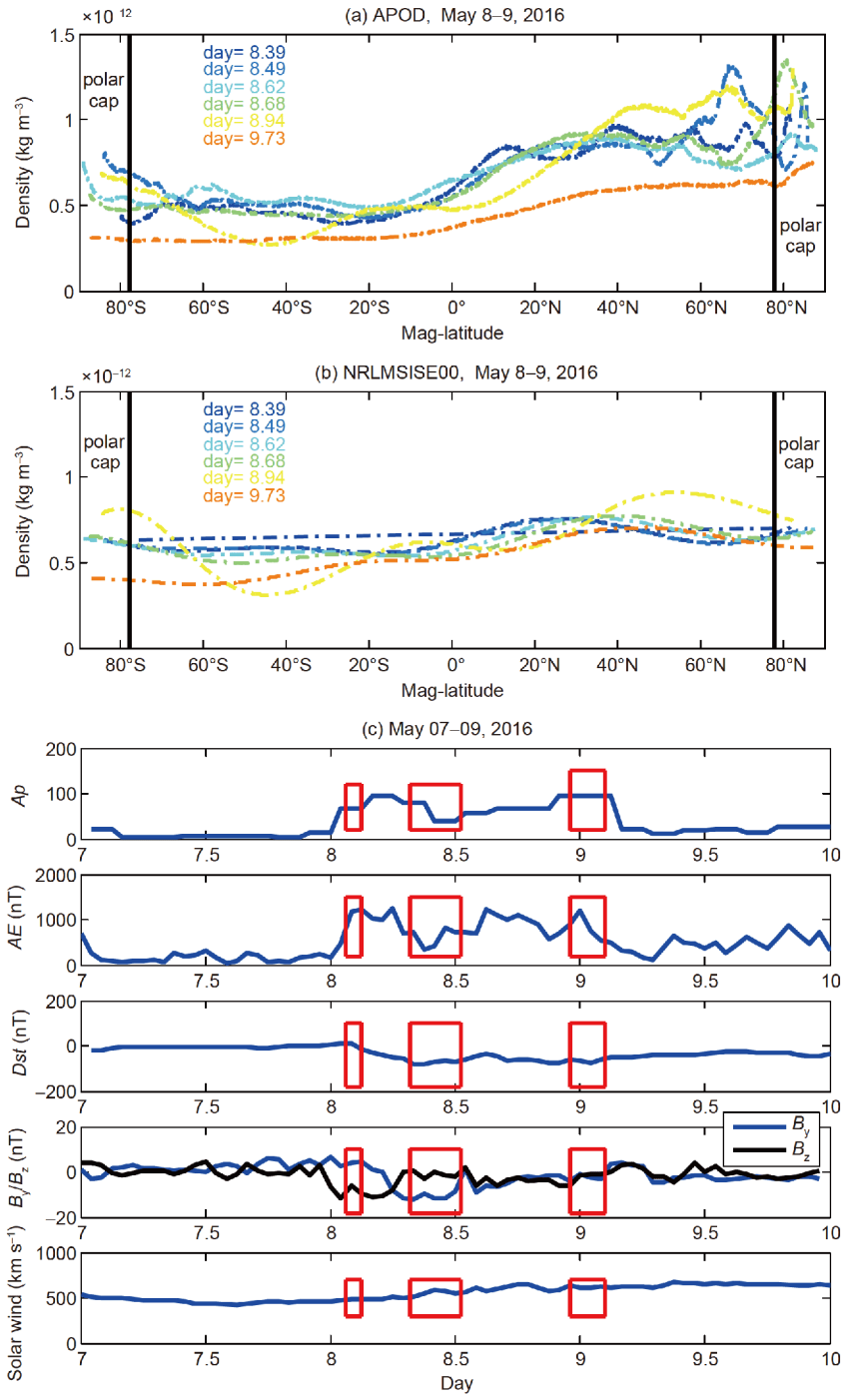

Figure 5 Same as Figure 4, but for the storm on May 8–9, 2016.

tellites.

The Polar region is a locus of significant energy transfer from ions and energetic particles to neutrals during magnetic storms (Huang et al., 2016). From *in-situ* observations of APOD, enhancements in the Polar region are found during several geomagnetic storms in the years 2015–2016. This phenomenon has been previously investigated by several authors from CHAMP and GRACE accelerometer-based estimates. For instance, 90% of 29 geomagnetic storms from 2002 to 2005 produces density enhancements in the polar region in Liu et al. (2010).

In this study, if the maximum of density arises over 20% from the prevailing background density, it is regarded as a density enhancement event. Figure 4 shows density variations for several orbits for the geomagnetic storm occurred December 20–21, 2015. Figure 4a shows the density esti-

mated by the APOD mission, and Figure 4b shows density estimates from NRLMSISE00. Density enhancements at the polar region show especially strong values in southern hemisphere, most probably due to the annual variation. In contrast, the phenomenon is not well represented by the NRLMSISE00 model. Similar results are shown in Figure 5 for the geomagnetic storm occurred on May 8–9, 2016. In this case, stronger enhancements are shown in the northern hemisphere as expected.

The Polar aurora region is a small area, and the anomalies are about medium scale size (typically <900 km). Fortunately, the high resolution of ADD density estimates (1 s) can provide representation in detail of enhancements. Since neutral mass density anomalies in the polar region usually only occur during magnetic storms, space weather parameters help to better understand the possible drivers and dependencies. We therefore investigate geomagnetic and space weather conditions during these geomagnetic storms. Figures 4c and 5c show the geomagnetic and space weather indexes during the corresponding geomagnetic storms. Occurrence of enhancements at the polar region is marked by red rectangles. We find that while enhancements occur, the *Ap* and *AE* indices reach maximum values, and the *Dst* and B_Z indices show minimum values. In this case, the increased neutral density is the evidence of localized Joule heating and energy input through particle precipitation and electric currents. We may conclude that electromagnetic energy input during geomagnetic storms is not restricted to the auroral zones (Huang et al., 2016).

5. Summary

The APOD project demonstrates the excellent potential of low-cost CubeSats for detecting thermospheric neutral mass density estates, and the possible spatiotemporal coverage extension with more available satellites in the future. The preliminary results of orbit determination have been validated with different methods and using independent data sources. The results show that the 3-D precision of APOD satellite position is better than 10 cm. After calibrating APOD-derived densities with POD drag-derived density, the accuracy of the density estimates is about 10% of the background density. The new semiannual variation recently included in the JB2008 semiempirical model is well represented by APOD estimates. In addition we represent density enhancements in the polar region during geomagnetic storms. The results demonstrate that APOD satellite an products are very useful to study thermosphere density variations. In the following years, along the decay of the APOD orbit, the *in-situ* ADD density estimates will play a great role in scientific community.

Acknowledgements *The authors would like to thank the ILRS for SLR data of the APOD mission. This work was supported by the National Natural Science Foundation of China (Grant Nos. 41874183, 41474131 & 41604131).*

References

Altamimi Z, Collilieux X, Métivier L. 2011. ITRF2008: An improved solution of the international terrestrial reference frame. J Geod, 85: 457–473

Bowman B R, Tobiska K, Marcos F, Huang C, Lin C, Burke W. 2008. A new empirical thermospheric density model JB2008 using new solar and geomagnetic indices. Hinolulu: AIAA/AAS Astrodynamics Specialist Conference and Exhibit, Guidance, Navigation, and Control and Co-located Conferences

Bruinsma S. 2015. The DTM-2013 thermosphere model. J Space Weather Space Clim, 5: A1

Bruinsma S L, Doornbos E, Bowman B R. 2014. Validation of GOCE densities and thermosphere model evaluation. Adv Space Res, 54: 576–585

Bruinsma S, Tamagnan D, Biancale R. 2004. Atmospheric densities derived from CHAMP/STAR accelerometer observations. Planet Space Sci, 52: 297–312

Calabia A, Jin S. 2016. New modes and mechanisms of thermospheric mass density variations from GRACE accelerometers. J Geophys Res-Space Phys, 121: 11191–11212

Calabia A, Jin S G. 2017. Thermospheric density estimation and responses to the March 2013 geomagnetic storm from GRACE GPS-determined precise orbits. J Atmos Sol-Terr Phys, 154: 167–179

Chen G M, Xu J, Wang W, Burns A G. 2014. A comparison of the effects of CIR- and CME-induced geomagnetic activity on thermospheric densities and spacecraft orbits: Statistical studies. J Geophys Res-Space Phys, 119: 7928–7939

Clemmons J H, Friesen L M, Katz N, Ben-Ami M, Dotan Y, Bishop R L. 2009. The ionization gauge investigation for the streak mission. Space Sci Rev, 145: 263–283

Doornbos E, van den IJssel J, Luehr H, Foerster M, Koppenwallner G, Bruinsma S, Sutton E, Forbes J M, Marcos F, Perosanz F. 2010. Neutral density and crosswind determination from arbitrarily oriented multiaxis accelerometers on satellites. J Spacecraft Rockets, 47: 580–589

Emmert J T. 2015. Thermospheric mass density: A review. Adv Space Res, 56: 773–824

Gu D, Liu Y, Yi B, Cao J, Li X. 2017. In-flight performance analysis of MEMS GPS receiver and its application to precise orbit determination of APOD-A satellite. Adv Space Res, 60: 2723–2732

Gurtner W, Noomen R, Pearlman M R. 2005. The international laser ranging service: Current status and future developments. Adv Space Res, 36: 327–332

Hedin A E, Biondi M A, Burnside R G, Hernandez G, Johnson R M, Killeen T L, Mazaudier C, Meriwether J W, Salah J E, Sica R J, Smith R W, Spencer N W, Wickwar V B, Virdi T S. 1991. Revised global model of thermosphere winds using satellite and ground-based observations. J Geophys Res, 96: 7657–7688

Huang C, Huang Y, Su Y, Sutton E K, Hairston M R, Coley W R. 2016. Ionosphere-thermosphere (IT) response to solar wind forcing during magnetic storms. J Space Weather Space Clim, 6: A4

Li X, Xu J Y, Tang G S, Chen G M, Man H Y, Liu S S, Li Y P. 2018. Processing and calibrating of *in-situ* atmospheric densities for APOD (in Chinese). Chin J Geophys, 61: 3567–3576

Liu H, Lühr H. 2005. Strong disturbance of the upper thermospheric density due to magnetic storms: CHAMP observations. J Geophys Res, 110: A09S29

Liu R, Lühr H, Ma S Y. 2010. Storm-time related mass density anomalies in the polar cap as observed by CHAMP. Ann Geophys, 28: 165–180

Pearlman M R, Degnan J J, Bosworth J M. 2002. The international laser ranging service. Adv Space Res, 30: 135–143

Picone J M, Emmert J T, Lean J L. 2005. Thermospheric densities derived from spacecraft orbits: Accurate processing of two-line element sets. J Geophys Res, 110: A03301

Picone J M, Hedin A E, Drob D P, Aikin A C. 2002. NRLMSISE-00 empirical model of the atmosphere: Statistical comparisons and scientific issues. J Geophys Res, 107: SIA 15-1–SIA 15-16

Qian L, Solomon S C. 2012. Thermospheric density: An overview of temporal and spatial variations. Space Sci Rev, 168: 147–173

Qin G, Xu G, Ma Z. 1990. Satellite-borne ionization gauge measures upper atmospheric densities. Res Space Phys, 5: 143–149

Sang J, Smith C, Zhang K. 2012. Towards accurate atmospheric mass density determination Using precise positional information of space objects. Adv Space Res, 49: 1088–1096

Storz M F, Bowman B R, Branson M J I, Casali S J, Tobiska W K. 2005. High accuracy satellite drag model (HASDM). Adv Space Res, 36: 2497–2505

Sutton E K, Forbes J M, Nerem R S. 2005. Global thermospheric neutral density and wind response to the severe 2003 geomagnetic storms from CHAMP accelerometer data. J Geophys Res, 110: A09S40

Willis P, Deleflie F, Barlier F, Bar-Sever Y E, Romans L J. 2005. Effects of thermosphere total density perturbations on LEO orbits during severe geomagnetic conditions (Oct–Nov 2003) using DORIS and SLR data. Adv Space Res, 36: 522–533

Xu J, Wang W, Lei J, Sutton E K, Chen G. 2011. The effect of periodic variations of thermospheric density on CHAMP and GRACE orbits. J Geophys Res, 116: A02315

(Responsible editor: Jiyao XU)